Anisotropic dispersion with a consistent smoothed particle hydrodynamics scheme

Carlos E. Alvarado-Rodríguez[a,b], Leonardo Di G. Sigalotti[c,*], Jaime Klapp[b]

[a] *Departamento de Ingeniería Química, DCNyE, Universidad de Guanajuato, Noria Alta S/N, 36000 Guanajuato, Guanajuato, Mexico*

[b] *Departamento de Física, Instituto Nacional de Investigaciones Nucleares (ININ), Carretera México-Toluca km. 36.5, La Marquesa, 52750 Ocoyoacac, Estado de México, Mexico*

[c] *Área de Física de Procesos Irreversibles, Departamento de Ciencias Básicas, Universidad Autónoma Metropolitana-Azcapotzalco (UAM-A), Av. San Pablo 180, 02200 Ciudad de México, Mexico*

Abstract

A consistent smoothed particle hydrodynamics (SPH) approach is used to simulate the anisotropic dispersion of a solute in porous media. Consistency demands using large numbers of neighbors with increasing resolution. The method is tested against the anisotropic dispersion of a Gaussian contaminant plume. Using irregularly distributed particles, the solution for isotropic dispersion converges to second-order accuracy when at sufficiently high resolution a large number of neighbors is used within the kernel support. For low to moderate anisotropy, the convergence rates are close to second-order, while for unusually large anisotropic dispersion the solutions converge to better than first-order. When negative concentrations arise, they are several orders of magnitude smaller than those encountered with standard SPH and comparable to those obtained with the MWSPH scheme of Avesani *et al.* The method is also insensitive to particle disorder and achieves an overall accuracy comparable to the MWSPH method using a much simpler approach.

Keywords: Particle method, transport, advection-diffusion, anisotropic dispersion, porous media

*Corresponding author

Email addresses: iqcarlosug@gmail.com (Carlos E. Alvarado-Rodríguez), leonardo.sigalotti@gmail.com (Leonardo Di G. Sigalotti), jaime.klapp@inin.gob.mx (Jaime Klapp)

1. Introduction

Solute transport through heterogeneous porous media is observed in a wide variety of natural processes and industrial applications, which span the design of oil recovery strategies to the development of packed bed reactors in chemical plants to the establishment of fluid flow potential through construction materials. Solute transport is also observed in the spread of contaminants in subsurface water [1] and the transport of nutrients in soil water [2].

In general, the migration of solutes in a geological medium is governed by three different mechanisms, namely fluid advection, molecular diffusion and mechanical (or hydrodynamical) dispersion. Advection causes the translation of the solute field with the flow velocity, while diffusion is independent of the flow and describes the spread of the solute due to the presence of concentration gradients. On the other hand, mechanical dispersion is caused by the different flow paths that fluid particles take due to the heterogeneity of the porous medium. It is therefore a property characteristic of the porous medium and can be considered to materialize the tortuosity of the particle trails due to the random arrangement and the interconnectivity of the channels constituting the pore space. Mechanical dispersion is in general assumed to obey Fick's law [3] and it is known to increase linearly with increasing fluid pore velocity, except at low velocities where molecular diffusion dominates [4, 5, 6]. Dispersive transport occurs in three directions, i.e., parallel to the main flow (longitudinal dispersion) and along the other two orthogonal directions perpendicular to the main flow (transverse dispersion). In general, the spreading of the solute is anisotropic, with the transverse dispersion being at least an order of magnitude smaller than the longitudinal dispersion [3].

Solute transport by the simultaneous action of these three mechanisms usually rely on numerical solutions of the classical advection-dispersion equation (ADE) coupled to the mass and momentum conservation laws [3]. For instance, in contaminant hydrology it is often assumed that the transport can be modeled as a flow in a homogeneous domain with some dispersion coefficient designed to accommodate the molecular diffusion and the dispersion of the contaminant due to small-scale heterogeneity. In mathematical form, the dispersion coefficient in anisotropic media is represented by a tensor of second rank [3]. This together with the rapid changes in magnitude

and direction of the flow velocity in geological formations, make the numerical prediction of anisotropic dispersion with traditional finite-difference and finite-volume methods very difficult. Such numerical solutions were found to suffer from unphysical oscillations and negative concentrations when dispersion is strongly anisotropic and the principal direction of dispersion deviates significantly from the grid orientation [7, 8, 9, 10, 11].

On the other hand, only a few studies have assessed the use of particle methods to simulate anisotropic dispersion [12, 13, 14, 15, 16]. Because of their Lagrangian character, particle methods are free of numerical dispersion and artificial mixing when simulating flow advection and so they appear to be better suited than traditional grid-based methods to simulate solute dilution and mixing. In particular, Zimmermann *et al.* [12] evaluated the performance of the particle strength exchange (PSE) method [17] to simulate anisotropic dispersion in a homogeneous porous medium under uniform and nonuniform flow conditions, finding acceptably accurate results only when a Lagrangian-distortion re-meshing step was employed to correct for the flow field topology leading to clustering or spreading. An alternative particle method to the PSE scheme was proposed by Beaudoin *et al.* [13] based on the diffusion velocity concept [18]. However, compared to the PSE scheme, this method gains in robustness and simplicity at the price of losing accuracy. Later on, Herrera *et al.* [14] modeled the isotropic dispersion in heterogeneous porous media with the aid of standard smoothed particle hydrodynamics (SPH), obtaining results comparable to those from grid-based techniques. They found that no re-meshing procedure is necessary if the second-order derivatives are approximated in terms of only first-order derivatives of the kernel function, as is currently done in most SPH applications to reduce the sensitivity to particle disorder [19]. More recently, Herrera and Beckie [15] tested their SPH scheme against a benchmark problem of anisotropic dispersive transport and performed direct comparison of their results with an implementation of the PSE method and a standard finite volume scheme. With all three methods, the numerical solutions were seen to exhibit artificial oscillations and negative concentrations when the off-diagonal terms of the tensorial dispersion coefficient are nonzero. Also, the solutions exhibited larger errors and slower convergence rates compared to the isotropic case. They concluded that the non-linear amplification of these oscillations represents a severe drawback for flow simulations where the anisotropic nature of the dispersion tensor must be considered. To cope with this difficulty, Avesani *et al.* [16] proposed a modified version of the standard SPH scheme based on a Moving-Least-

Squares-Weighted-Essentially-Non-Oscillatory (MLS-WENO) reconstruction of concentrations, referred to as the MWSPH method, which produced accurate results and a drastic reduction of unphysical oscillations compared to previous SPH calculations.

The lesson that emerged from Herrera and Beckie's [15] work is that the accuracy of dispersive transport simulations with standard SPH is highly sensitive to the spatial distribution of particles. In general, the accuracy declines as the degree of particle disorder increases, even for isotropic diffusion-dispersion models. However, the calculations of Avesani *et al.* [16] have also shown that the MWSPH method is rather insensitive to the spatial distribution of particles, which solves the drawback of standard SPH when applied to dispersive transport in the presence of heterogenoeus velocity fields. However, the considerable gain of accuracy of the MWSPH method is associated with an increase of the computational cost due to the intermediate steps involved in the MLS-WENO reconstruction and stencils construction. At comparable spatial resolution, the MWSPH scheme demands up to two orders of magnitude more CPU time than standard SPH [16]. Here we propose an alternative SPH scheme to the MWSPH method for dispersive transport calculations that corrects for the effects of particle disorder and reaches comparable limits of the absolute value of negative concentrations. The proposed scheme achieves comparable overall accuracy to the MWSPH method at approximately the same computational cost, but using a much simpler approach. The method is based on consistency considerations in standard SPH [20], where the number of neighbors (n) and the smoothing length (h) are initially set in terms of the total number of particles (N) by means of scaling relations that comply with the asymptotic limits $n \to \infty$, $h \to 0$ and $N \to \infty$ for complete SPH consistency as the spatial resolution is increased [21, 22]. The consistency (and accuracy) of SPH improves as the number of neighbors is increased with resolution, which is consistent with the expected dependence of the SPH particle discretization errors on $\sim 1/n$ [23, 24]. In particular, the error analysis of the SPH representations of the continuity and momentum equations performed by Read *et al.* [24] demonstrated that this error contributes with zeroth-order terms that would persist when working with a fixed, low number of neighbors even though $N \to \infty$ and $h \to 0$, causing a complete loss of particle consistency. Therefore, it is of interest to investigate whether the modified SPH method with varied number of neighbors will improve the accuracy and convergence rate of diffusion-dispersion transport simulations. When particle consistency is restored, the numerical

solutions become insensitive to particle disorder and the estimates of the function and its first derivatives converge essentially at the same rate [20]. However, nothing has been concluded in previous analyses on the consistency of the SPH approximations for second-order derivatives (which are key in the approximation of the diffusion-dispersion operator), except for their well-known reduced sensitivity to particle disorder when they are expressed in terms of first-order derivatives of the kernel function [19].

The plan of the paper is as follows. The mathematical model is given in Section 2, while Sections 3 and 4 describe the SPH formulation and the details of the numerical simulations, respectively. The results of the test simulations are given in Section 5 and the conclusions are contained in Section 6.

2. Mathematical formulation

Non-reactive solute transport in porous media is currently described by the ADE, which in Lagrangian coordinates can be written as

$$\frac{d\mathbf{x}}{dt} = \mathbf{v}, \tag{1}$$

$$\frac{dC}{dt} = \nabla \cdot (\mathbb{D} \cdot \nabla C) - C \nabla \cdot \mathbf{v}, \tag{2}$$

where $\mathbf{v} = \mathbf{v}(\mathbf{x}, t)$ is some external flow velocity vector, $C = C(\mathbf{x}, t)$ is the scalar tracer concentration, and $\mathbb{D}$ is a symmetric tensor of second rank defining the diffusion and dispersion coefficient. In component form, the diffusion and dispersion coefficient is defined by the relation [25, 3]

$$D_{ij} = (\alpha_{\mathrm{T}} |\mathbf{v}| + D_{\mathrm{m}})\, \delta_{ij} + (\alpha_{\mathrm{L}} - \alpha_{\mathrm{T}})\, \frac{v_i v_j}{|\mathbf{v}|}, \tag{3}$$

where α_{L} is the longitudinal dispersivity, α_{T} is the transverse dispersivity, D_{m} is the molecular diffusion coefficient and δ_{ij} is the Kronecker delta. In general, $\alpha_{\mathrm{T}} < \alpha_{\mathrm{L}}$ by at least an order of magnitude so that hydrodynamical dispersion is anisotropic [3]. It is clear from relation (3) that the dispersion coefficient depends on the magnitude and direction of the pore fluid velocity as well as on the ratio $\alpha_{\mathrm{T}}/\alpha_{\mathrm{L}}$. If $\alpha_{\mathrm{T}} = 0$, relation (3) becomes

$$D_{ij} = D_{\mathrm{m}} \delta_{ij} + \alpha_{\mathrm{L}} \frac{v_i v_j}{|\mathbf{v}|}, \tag{4}$$

for dispersion along the longitudinal direction only. Moreover, when $\alpha_{\rm T} = \alpha_{\rm L} = \alpha$, the off-diagonal terms of tensor D_{ij} vanish and the dispersion is isotropic with

$$D_{ij} = (\alpha|\mathbf{v}| + D_{\rm m})\,\delta_{ij}. \tag{5}$$

In two-space dimensions (2D), the components of tensor D_{ij} as defined by relation (3) in Cartesian coordinates are

$$\begin{aligned} D_{xx} &= \alpha_{\rm T}|\mathbf{v}| + D_{\rm m} + (\alpha_{\rm L} - \alpha_{\rm T})\,\frac{v_x^2}{|\mathbf{v}|}, \\ D_{xy} &= D_{yx} = (\alpha_{\rm L} - \alpha_{\rm T})\,\frac{v_x v_y}{|\mathbf{v}|}, \\ D_{yy} &= \alpha_{\rm T}|\mathbf{v}| + D_{\rm m} + (\alpha_{\rm L} - \alpha_{\rm T})\,\frac{v_y^2}{|\mathbf{v}|}, \end{aligned} \tag{6}$$

with $|\mathbf{v}| = (v_x^2 + v_y^2)^{1/2}$. For incompressible flow $\nabla \cdot \mathbf{v} = 0$, and so Eqs. (1) and (2) are coupled through the dispersion coefficient. Thus, for a time and space varying velocity field, the anisotropic dispersion will also be time and space varying.

3. SPH formulation

A SPH approximation for Eq. (2) can be constructed by first looking at the discretization form of the term $\nabla \cdot (\mathbb{D} \cdot \nabla C)$. Following Herrera and Beckie [15], this term satisfies the identity

$$\sum_{i=1}^{m}\sum_{j=1}^{m}\frac{\partial}{\partial x_i}\left(D_{ij}\frac{\partial C}{\partial x_j}\right) = \frac{1}{2}\sum_{i=1}^{m}\sum_{j=1}^{m}\left[\frac{\partial^2}{\partial x_i \partial x_j}\left(D_{ij}C\right) - C\frac{\partial^2 D_{ij}}{\partial x_i \partial x_j} + D_{ij}\frac{\partial^2 C}{\partial x_i \partial x_j}\right], \tag{7}$$

in index notation, where $m = 2$ in 2D and $m = 3$ in three dimensions (3D). According to this, the SPH discretization of the diffusion-dispersion operator reduces to estimating second-order derivatives of a scalar function. A general SPH approximation for the second-order derivative of a continuous function $f = f(\mathbf{x})$ at the position of particle a, say $\mathbf{x}_a$, has the form

$$\left(\frac{\partial^2 f}{\partial x_i \partial x_j}\right)_a = \sum_{b=1}^{n}\frac{m_b}{\rho_b}\left(f_a - f_b\right)\left(\Gamma\frac{x_{i,ab}x_{j,ab}}{|\mathbf{x}_{ab}|^2} - \delta_{ij}\right)\frac{1}{|\mathbf{x}_{ab}|^2}\mathbf{x}_{ab}\cdot\nabla_a W_{ab}, \tag{8}$$

where $\mathbf{x}_{ab} = \mathbf{x}_a - \mathbf{x}_b$, $|\mathbf{x}_{ab}|^2 = \mathbf{x}_{ab} \cdot \mathbf{x}_{ab}$, $W_{ab} = W(|\mathbf{x}_{ab}|, h)$ is the kernel function, and $\Gamma = 4$ in 2D and $\Gamma = 5$ in 3D. A formal derivation of the approximation (8) is given by Yildiz *et al.* [26]. For $i = j$, we find that

$$\sum_{i=1}^{m} \sum_{j=1}^{m} \left(\Gamma \frac{x_{i,ab} x_{j,ab}}{|\mathbf{x}_{ab}|^2} - \delta_{ij} \right) = \sum_{i=1}^{m} \left(\Gamma \frac{x_{i,ab} x_{i,ab}}{|\mathbf{x}_{ab}|^2} - \delta_{ii} \right) \to 2, \tag{9}$$

and so the double sum of Eq. (8) over i and j reduces to the SPH Laplacian approximation, which was found in Ref. [27] to be less sensitive to particle disorder than the more direct Laplacian form written in terms of second-order derivatives of the kernel function.

Substitution of Eq. (8) into Eq. (7), with $f \to D_{ij}C$, $f \to D_{ij}$ and $f \to C$, leads after some algebraic steps to the SPH representation of the dispersive term, which at the position of particle a reads as follows

$$\left[\nabla \cdot (\mathbb{D} \cdot \nabla C) \right]_a = \frac{1}{2} \sum_{b=1}^{n} \frac{m_b}{\bar{\rho}_{ab}} \mathcal{D}_{ab} \frac{(C_a - C_b)}{|\mathbf{x}_{ab}|^2} \mathbf{x}_{ab} \cdot \nabla_a W_{ab}, \tag{10}$$

where $\bar{\rho}_{ab} = (\rho_a + \rho_b)/2$ and

$$\mathcal{D}_{ab} = \sum_{i=1}^{m} \sum_{j=1}^{m} \frac{4 D_{ij,a} D_{ij,b}}{D_{ij,a} + D_{ij,b}} \left[\Gamma \frac{x_{i,ab} x_{j,ab}}{|\mathbf{x}_{ab}|^2} - \delta_{ij} \right]. \tag{11}$$

In the final steps of the above derivation the term $(D_{ij,a} + D_{ij,b})$ appearing in the definition of $\mathcal{D}_{ab}$ has been replaced by the ratio $4D_{ij,a}D_{ij,b}/(D_{ij,a}+D_{ij,b})$ of the geometrical over the arithmetic means of tensor component D_{ij} between particles a and b in order to guarantee continuity of the dispersive term when D_{ij} is discontinuous [19].

Finally, the convective term $C\nabla \cdot \mathbf{v}$ on the right-hand side of Eq. (2) is written in SPH form using the standard approximation

$$\left(C \nabla \cdot \mathbf{v} \right)_a = C_a \sum_{b=1}^{n} \frac{m_b}{\bar{\rho}_{ab}} \sum_{i=1}^{m} \left[\left(v_{x_i,b} - v_{x_i,a} \right) \frac{\partial W_{ab}}{\partial x_{i,a}} \right]. \tag{12}$$

For spreading of the solute in an external, spatially uniform velocity field this term vanishes identically and Eq. (2) reduces to a pure diffusion-dispersion equation.

3.1. SPH consistency

The concept of consistency is related to how closely the discrete equations approximate the exact differential equations. In particular, if a SPH approximation can reproduce an mth-order polynomial exactly, we say that the SPH approximation has C^m-consistency, or $(m+1)$th-order accuracy. The standard SPH method is known to have C^0 and C^1 kernel consistency for conventional kernel functions. However, satisfaction of these kernel consistency conditions does not imply that C^0 and C^1 particle consistency is also satisfied by the corresponding SPH approximation. This discrepancy between the kernel and particle approximations is what we mean in SPH by loss of the particle consistency. It is well-known that standard SPH does not even have C^0 particle consistency due to violation of the discrete normalization condition of the kernel. The loss of consistency in the particle approximation procedure is usually associated with (a) the truncation of the kernel function at and near a physical domain boundary, (b) the particle disorder and (c) the use of temporally and spatially varying smoothing lengths [28].

It was not until recently that Zhu *et al.* [22] identified another source of particle inconsistency associated with the fixed, low number of neighbors within the compact support of the kernel function (it has been common practice in SPH simulations to use low numbers of neighbors (≤ 60) independently of the total number of particles). They showed that C^0 particle consistency can be achieved only when n is sufficiently large so that the zeroth-order error term carried by the SPH discretization declines [24], making the SPH sum approximation to approach the continuous kernel approximation limit. For $n \gg 1$, Zhu *et al.* [22] parameterized this error as $\sim 1/n^\gamma$, where $\gamma = 0.5$ for randomly distributed particles and $\gamma = 1$ for low-discrepancy sequences of particles (i.e., pseudo-random distributions) as is more appropriate for SPH. Based on a balance between the leading error of the kernel approximation ($\propto h^2$ as is appropriate for most commonly used kernels) and the $\sim 1/n^\gamma$ error of the particle approximation, Zhu *et al.* [22] derived the scaling relations $n \propto N^{1-3/\beta}$ and $h \propto N^{-1/\beta}$ for $\beta \in [5, 7]$, which satisfy the joint limit $N \to \infty$, $h \to 0$ and $n \to \infty$, with $n/N \to 0$ [21], for full particle consistency when N is increased. A recent analysis has demonstrated that with the use of the above scaling relations, C^0-consistency is restored for both the particle estimates of a function and its first-order derivatives, with the numerical solution becoming insensitive to particle disorder and the effects of domain boundaries [20]. In passing we note that if C^0 particle consistency

is achieved, C^1 particle consistency is also guaranteed because of the kernel symmetry.

An intermediate value of $\beta = 6$ is appropriate when the smoothing is performed on pseudo-randomly distributed particles. For the simulations of this paper we then allow h to vary with N as $h = N^{-1/6}$. With this choice, a family of curves can be obtained for the dependence of n on N. Out of the set of possible curves, we have chosen the scaling relations $n \approx 2.81N^{0.675}$ and $h \approx 1.29n^{-0.247}$ to set the initial values of n and h in terms of N. These exponents are slightly larger than the reference values of 0.5 and $-1/3$ when $\beta = 6$. With this choice, large numbers of neighbors can be accommodated for a given N while keeping reasonably large values of h. However, other choices with exponents closer to, or even slightly smaller than, the reference values produced convergence rates of the numerical solutions that remained essentially the same [20].

3.2. The kernel function

Most commonly used kernels cannot support arbitrarily large number of neighbors because for finite-sized smoothing lengths they suffer from the so-called pairing instability, which sets in when particles start to form pairs. In some extreme cases, the paired particles become so close to each other that they emerge as effectively one particle, leading to a loss of resolution while keeping the computational cost the same. A promising family of kernel functions which are free from the pairing instability and therefore show much better convergence properties than traditional kernels are the Wendland functions [29, 30]. Here we adopt the Wendland C^4 function, defined as [30]

$$W(q,h) = B(1-q)^6\left(1+6q+\frac{35}{3}q^2\right), \tag{13}$$

if $q \leq 1$ and 0 otherwise, where $q = |\mathbf{x}-\mathbf{x}'|/h$, $B = 9/(\pi h^2)$ in 2D and $B = 495/(32\pi h^3)$ in 3D. A kernel function of this type has a strictly positive Fourier transform and no inflection points. These are desirable properties for convergence studies since the neighbor number can be increased without limit. In addition, Wendland functions are reluctant to allow particle motion on sub-resolution scales, thereby maintaining very regular particle distributions, even in highly dynamical tests [31]. This is a further important concern for accuracy and convergence of the SPH method.

3.3. Time step control and time integration

Equations (1) and (2) are solved explicitly by means of a predictor-corrector leapfrog integration scheme. The time step control for numerical stability is set by the condition [15]

$$\Delta t \leq C_{\mathrm{T}} \frac{h^2}{\sum_{i=1}^{m} D_{ii}}, \tag{14}$$

so that the minimum Δt is taken over all particles. Herrera and Beckie [15] found through numerical experiments that their SPH solutions were stable if $C_{\mathrm{T}} = 0.1$. In order to provide a comparison with their solutions and evaluate the effects of improving the consistency of SPH when using arbitrarily large numbers of neighbors we use the same value for the constant C_{T}.

In the predictor step, particle positions and concentrations are evolved to an intermediate time $t^{l+1/2}$ through the sequence

$$\begin{aligned} \mathbf{x}_a^{l+1/2} &= \mathbf{x}_a^{l-1/2} + \Delta t \mathbf{v}_a^l, \\ C_a^{l+1/2} &= C_a^l + \frac{1}{2}\Delta t \left(\frac{dC}{dt}\right)_a^l. \end{aligned} \tag{15}$$

With these updates, the time rate of change of the concentration is calculated at the intermediate time level for use in the corrector step where quantities are advanced to the new time t^{l+1} according to

$$\begin{aligned} \mathbf{x}_a^{l+1} &= \mathbf{x}_a^l + \Delta t \mathbf{v}_a^{l+1/2}, \\ C_a^{l+1} &= C_a^l + \Delta t \left(\frac{dC}{dt}\right)_a^{l+1/2}. \end{aligned} \tag{16}$$

For the simulation cases of this paper, the flow velocity is given as an external constant input parameter and therefore $\mathbf{v}_a^l = \mathbf{v}_a^{l+1/2}$. In the more general case of a temporally and spatially varying velocity field, the continuity and momentum equations must be solved coupled to Eqs. (1) and (2), which can be easily accommodated in the above time integrator.

4. Numerical simulations

In this section, we analyze the accuracy of the method for 2D simulations of the anisotropic dispersion of a Gaussian pollutant source. The method is

applied to a benchmark diffusion-dispersion problem with analytical solution [12, 13, 15]. In particular, we test the performance of our SPH scheme by comparing the numerical results with those obtained by Avesani *et al.* [16] with their MWSPH method.

4.1. Model setup and initial conditions

The test consists of releasing instantaneously an initial Gaussian concentration of solute mass $\Delta M = 10^4$ kg given by

$$C(\mathbf{x}, t = 0) = C_0 \exp\left[\frac{-(x - x_0)^2 - (y - y_0)^2}{2w^2}\right], \tag{17}$$

in a two-dimensional unbounded domain with a temporally and spatially constant velocity field, where $C_0 = 0.32$ kg m^{-3} is the maximum initial concentration, $w = 44$ m is the width of the Gaussian plume at $t = 0$ and (x_0, y_0) are the coordinates of the plume center at $t = 0$. The unbounded domain is modeled by a square of side length $L = 2000$ m and by implementing periodic boundary conditions at its borders. The contaminant is injected at the center of the square so that $x_0 = y_0 = 1000$ m. Because of the constant flow velocity, the advective term on the right-hand side of Eq. (2) is identically zero and so the transport process will depend on the flow only through the relation between the dispersion coefficient and the flow velocity.

The analytical solution for the solute concentration at any time $t > 0$ is given by

$$\frac{C(\mathbf{x}, t)}{C_0} = \frac{w^2}{C_4} \exp\left[\frac{-(x - x_0)^2 A_1 - (y - y_0)^2 A_2 + 4(x - x_0)(y - y_0) A_3}{8t^2 C_2 + 4w^2 t C_3 + 2w^2}\right], \tag{18}$$

where

$$\begin{aligned} A_1 &= 2tD_{yy} + w^2, \\ A_2 &= 2tD_{xx} + w^2, \\ A_3 &= tD_{xy}, \\ C_2 &= D_{xx}D_{yy} - D_{xy}^2, \\ C_3 &= D_{xx} + D_{yy}, \\ C_4 &= \left(4t^2 C_2 + 2tw^2 C_3 + w^4\right)^{1/2}. \end{aligned} \tag{19}$$

The longitudinal dispersivity is $\alpha_{\mathrm{L}} = 10$ m and the constant flow velocity is taken to be $v = \sqrt{v_x^2 + v_y^2} = 1$ m day^{-1} ($\approx 1.16 \times 10^{-5}$ m s^{-1}). In addition,

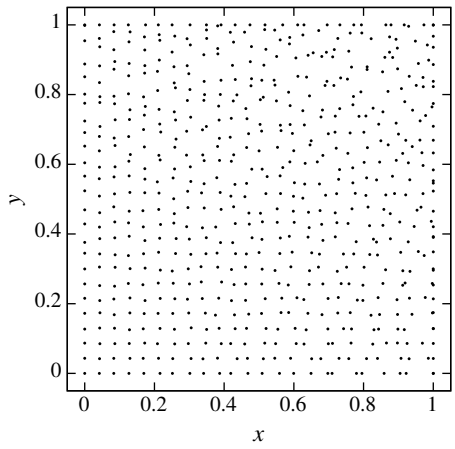

Figure 1: Irregular particle distribution for the lowest resolution runs with $N = 625$ particles and $n = 217$ neighbors within the kernel support. The side lengths of the square domain are normalized to $L = 2000$ m. The same pattern is also employed for the higher resolution runs.

the molecular diffusivity D_{m} in Eq. (3) is set to zero and so the dispersion tensor will only depend on the longitudinal and transverse dispersivities and on the magnitude and direction of the flow velocity.

4.2. Simulation cases

For all simulations, the square domain is filled with irregularly distributed particles following a low-discrepancy (i.e., quasi-random) sequence. We will study the convergence rate of our modified SPH scheme for four different dispersivity ratios $\alpha_{\mathrm{T}}/\alpha_{\mathrm{L}}$ and two different flow orientations with increasing number of neighbors and decreasing smoothing lengths as the resolution is increased, according to the scaling relations defined in Section 3.1. Table 1 lists the spatial resolution parameters. The first four columns list the mean particle separation distance normalized to L, the total number of SPH particles, the corresponding number of neighbors and the smoothing lengths normalized to L, respectively, while the fifth column gives the CPU time (in seconds) of the code on an Intel(R) Xeon E5-2690 v3 CPU, Clockspeed 2.6 GHz processor with 12 cores. As an example of the initial irregular particle distribution, Fig. 1 shows the placement of particles for the lowest resolution case ($N = 625$). The same degree of particle disorder is employed for all

other runs of Table 1. In Fig. 1, the coordinates of particle positions are normalized to the side length, L, of the square domain. A gradient of the degree of particle disorder is evident in Fig. 1, where in the bottom left the particles are in a quasi-regular array, while toward the upper right they make a transition to a much more disordered distribution.

Table 1: Spatial resolution parameters for the simulations.

Mean particle separation	Number of SPH particles	Number of neighbors	Smoothing length	CPU time
$\langle \Delta x \rangle / L$	N	n	h/L	t (s)
0.0420	625	217	0.342	0.40
0.0205	2500	552	0.271	2.62
0.0135	5625	955	0.237	8.99
0.0101	10000	1408	0.215	22.95
0.0067	22500	2435	0.188	103.71
0.00503	40000	3590	0.171	291.55
0.00335	90000	6206	0.149	1282.08
0.00251	160000	9151	0.136	2317.53
0.00201	250000	12368	0.126	5181.21
0.00134	562500	21382	0.110	25453.14
0.00100	1000000	31529	0.099	98766.54

We consider values of $\alpha_{\rm T}/\alpha_{\rm L} = 0.001$, 0.01, 0.1 and 1.0, where $\alpha_{\rm T}/\alpha_{\rm L} = 1.0$ corresponds to isotropic dispersion and $\alpha_{\rm T}/\alpha_{\rm L} = 0.001$ corresponds to very large anisotropic dispersion. In addition, we choose two different orientations for the external flow velocity, i.e., $\theta = 0^\circ$ and $\theta = 45^\circ$, measured with respect to the x-axis. With these choices, $v_x = v$ and $v_y = 0$ (for $\theta = 0^\circ$) and $v_x = v_y = \sqrt{2}v/2$ (for $\theta = 45^\circ$). In order to provide comparison with standard SPH and MWSPH simulations, the range of values of these parameters are the same employed by Herrera and Beckie [15] and Avesani *et al.* [16].

Equations (1) and (2) are solved in normalized form using the following prescriptions: $t \to t/(300$ days$)$, $C(\mathbf{x},t) \to C(\mathbf{x},t)/C_0$, $w \to w/L$, $\alpha_{\rm L} \to \alpha_{\rm L}/L$, $\alpha_{\rm T} \to \alpha_{\rm T}/L$, $x_0 \to x_0/L$, $y_0 \to y_0/L$, $v \to v/v_0$, $D_{xx} \to D_{xx}/(v_0 L)$, $D_{xy} \to D_{xy}/(v_0 L)$ and $D_{yy} \to D_{yy}/(v_0 L)$, where $v_0 = 20/3$ m days^{-1}. For each pair of values ($\alpha_{\rm T}/\alpha_{\rm L}$, θ) and the eleven resolutions of Table 1, the convergence study amounts to a total number of 88 independent runs. In all cases, the simulations were terminated after 300 days (i.e., normalized time

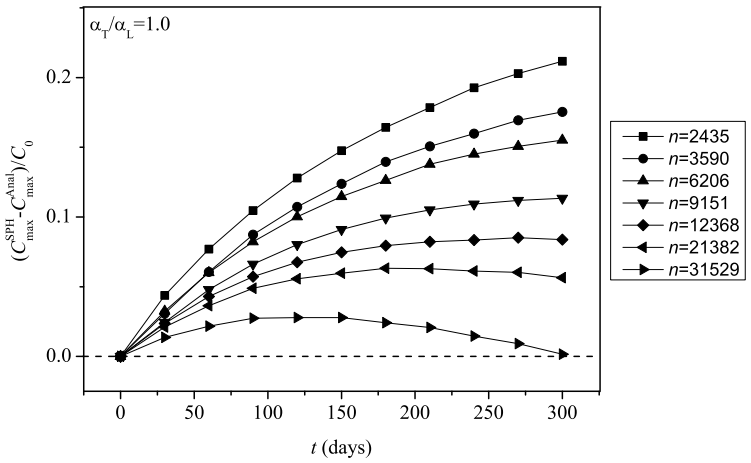

Figure 2: Difference of the maximum concentration values between the analytical and numerical solutions for the isotropic dispersion case ($\alpha_T/\alpha_L = 1.0$) as a function of time. The results for varying spatial resolutions are shown up to $t = 300$ days. The legends in the inset on the right of the figure identify the symbols on the curves with the spatial resolution in terms of the number of neighbors within the kernel support.

$t = 1$). The models were run using a modified version of the fully parallel, open-source code DualSPHysics for diffusive and dispersive transport problems, which relies on SPH theory for solving the fluid-dynamics equations [32, 33].

5. Results

5.1. Isotropic dispersion

We first consider the case of isotropic dispersion when $\alpha_T/\alpha_L = 1.0$. Figure 2 shows the difference of the maximum concentration values between the analytical and numerical solutions normalized to the maximum initial concentration C_0 as a function of time. The curves belong to different resolution runs for the same model and the symbols on each curve display the data at discrete intervals of about 30 days. As the resolution is increased, the difference in the maximum concentrations decreases. At $t = 300$ days, the relative errors drop from $\sim 18\%$ (when $N = 22500$ and $n = 2435$) to $\sim 0.2\%$ (when $N = 562500$ and $n = 21382$), reaching values lower than $\sim 0.04\%$ when the resolution is increased to $N = 1000000$ and $n = 31529$. The maximum

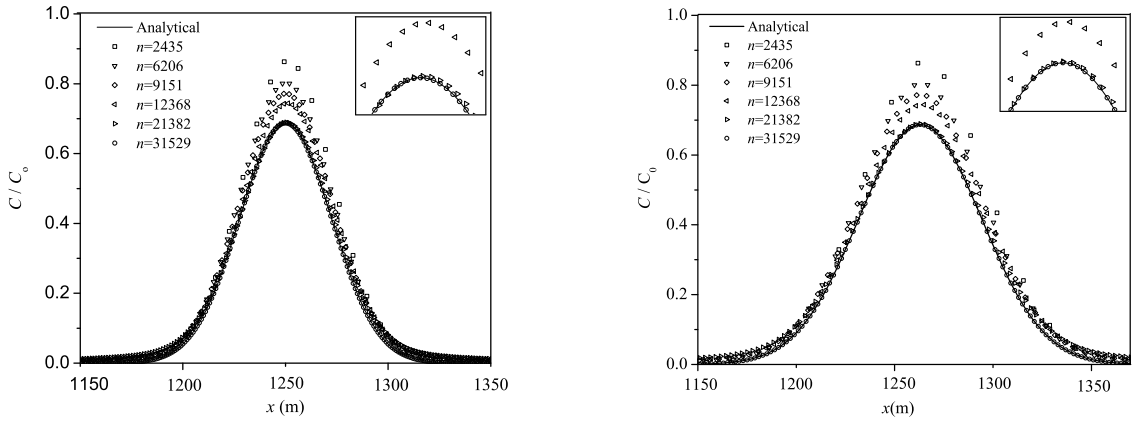

Figure 3: Concentration profiles at different spatial resolutions compared to the analytical solution (solid line) at $t = 300$ days for the isotropic case ($\alpha_{\mathrm{T}}/\alpha_{\mathrm{L}} = 1.0$) when $\theta = 0°$ (left) and $\theta = 45°$ (right).

relative errors are shifted to earlier times as the resolution is improved, with values ranging from $\sim 6\%$ to $\sim 2.2\%$ when n increases from 21382 to 31529. Hence, standard SPH is very sensitive to the choice of N and n, and therefore to the smoothing length since larger values of n correspond to smaller values of h. The trends shown in Fig. 2 are similar to those reported by Avesani *et al.* [16] in their Fig. 5, where the difference is seen to increase from the beginning, reaching a maximum value much earlier than predicted here and then decreasing to an asymptotic value at later times as the contaminant concentration smooths out. However, almost identical curves to those shown in Fig. 2 for $n = 21382$ and $n = 31529$ are obtained when these models are recalculated with perfectly uniform particle distributions, meaning that the numerical solution becomes insensitive to the degree of particle disorder when the zeroth-order discretization errors are reduced for large values of n.

As the number of neighbors is increased, the size of the smoothing length is decreased and the zeroth-order errors carried by the particle discretization decay as $\sim 1/n$, making the SPH approximation to become essentially insensitive to particle disorder [20]. When working with finite h, consistency demands that $n \to \infty$, while accuracy demands that $n \to \infty$ and $h \to 0$ in order to have convergent results in the limit $N \to \infty$. The choice of scaling relations slightly different to $n \approx 2.81N^{0.675}$ and $h \approx 1.29n^{-0.247}$, with exponents closer to 0.5 in the former case and to -0.33 in the latter case

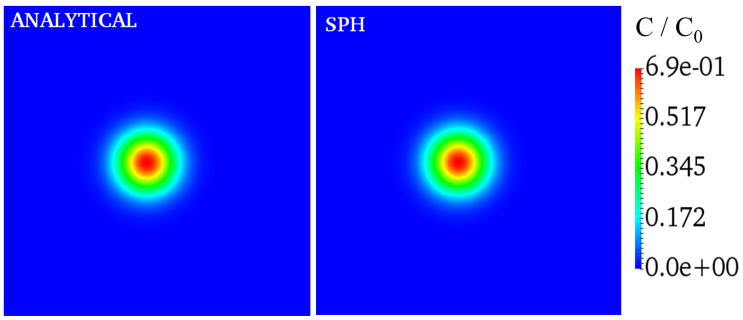

Figure 4: Concentration field resulting from the highest resolution run with $N = 1000000$ particles and $n = 31529$ neighbors as compared to the analytical solution at $t = 300$ days for the isotropic case ($\alpha_T/\alpha_L = 1.0$) and $\theta = 0°$. The color bar on the right indicates the magnitude of the concentration normalized to the maximum initial concentration for both frames.

will result in correspondingly smaller values of n and h at given N, thus improving the accuracy in terms of h and reducing the computational cost since less neighbors will fill the kernel support.

Figure 3 compares the concentration profiles for the isotropic case at different resolutions with the analytical solution (solid line) at $t = 300$ days when $\theta = 0°$ (left) and $\theta = 45°$ (right). In all cases, the profiles are shown along a section forming an angle of $0°$ with respect to the x-axis. Independently of the flow orientation, the numerical solution matches the analytical one everywhere when $N \geq 562500$ and $n \geq 21382$, with root-mean-square errors (RMSEs) that are less than $2.7 \times 10^{-4}\%$ (see Section 5.3). As the resolution decreases, the matching deteriorates particularly around the peak of the distribution, where the distance between the maximum analytical and numerical concentrations increases and the distribution becomes relatively broader. The concentration field for $\alpha_T/\alpha_L = 1.0$, with $N = 1000000$, $n = 31529$ and $\theta = 0°$ is shown in Fig. 4 as compared to the analytical solution at $t = 300$ days. The shape and structure of the contaminant plume are almost identical to the analytical solution and independent of the flow

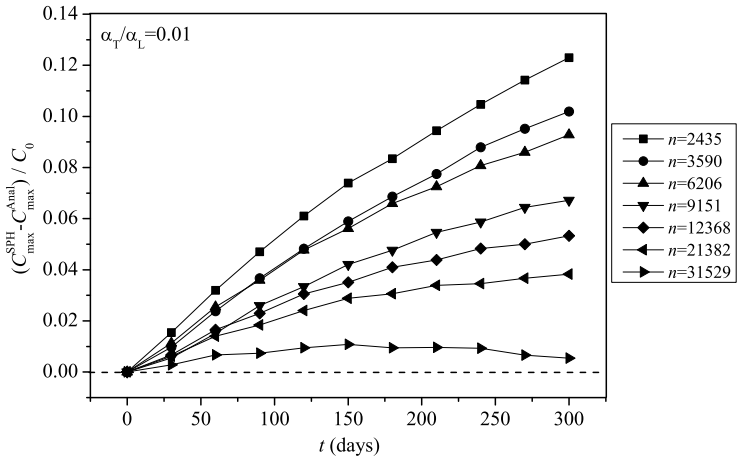

Figure 5: Difference of the maximum concentration values between the analytical and numerical solutions for the anisotropic dispersion case with $\alpha_T/\alpha_L = 0.01$ as a function of time. The results for varying spatial resolution are shown up to $t = 300$ days. The legends in the inset on the right of the figure identify the symbols on the curves with the spatial resolution in terms of the number of neighbors within the kernel support.

orientation. For the isotropic runs, including those with coarser resolutions, the numerical solution is always free from spurious oscillations that cause negative values of the concentration.

5.2. Anisotropic dispersion

We now explore the performance of the method when the dispersion is anisotropic, i.e., when the dispersivity ratio $\alpha_T/\alpha_L < 1$. In particular, Figs. 5 and 6 show the temporal variation of the difference of the maximum concentration values between the numerical and analytical solutions at various resolutions for the highly anisotropic cases $\alpha_T/\alpha_L = 0.01$ and 0.001, respectively. The differences are always positive independently of the resolution, meaning that SPH overestimates the maximum concentration. For the highest resolution run (i.e., for $N = 1000000$ and $n = 31529$), the maximum relative error at earlier times is smaller than 1% for both dispersivities, which is comparable with those reported by Avesani *et al.* [16] with their MWSPH-M3 and MWSPH-M4 models for irregularly distributed particles. At $t = 300$ days, the relative errors have decayed to less than 0.12% regardless of the value of α_T/α_L, meaning that good convergence is achieved by SPH at such

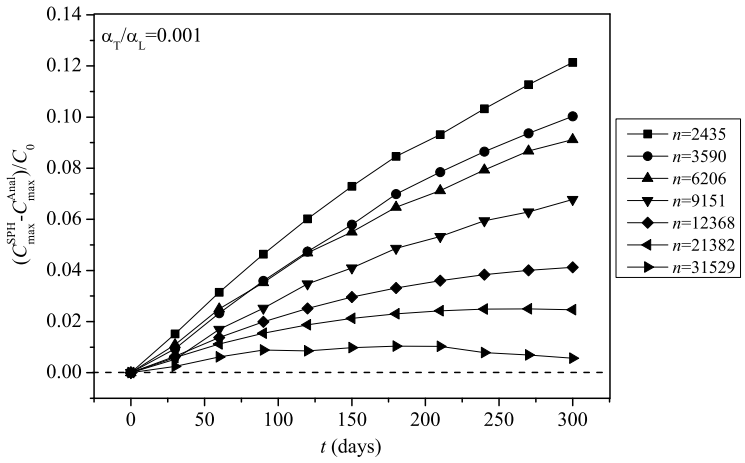

Figure 6: Difference of the maximum concentration values between the analytical and numerical solutions for the anisotropic dispersion case with $\alpha_{\mathrm{T}}/\alpha_{\mathrm{L}} = 0.001$ as a function of time. The results for varying spatial resolution are shown up to $t = 300$ days. The legends in the inset on the right of the figure identify the symbols on the curves with the spatial resolution in terms of the number of neighbors within the kernel support.

resolution independently of the dispersivity ratio. This behavior can be explained as follows. The combined kernel and particle discretization errors in SPH go as

$$\mathcal{E} \sim \frac{a_0}{n} + \frac{a_1 h}{n} + \left(\frac{a_2}{n} + a_2^{(K)}\right) h^2, \tag{20}$$

where the term proportional to $a_2^{(K)}$ is the contribution from the continuous kernel approximation, while the remaining zeroth-, first-, and second-order terms are the contributions from the particle discretization. For large n the error is dominated by the term $a_2^{(K)} h^2$, while for small h the main source of error is given by the zeroth-order term a_0/n. This term contributes with an irreducible error even when $N \to \infty$ and $h \to 0$. Thus, for finite values of h consistency is achieved only for sufficiently large values of n, while accuracy results from the additional requirement that h be sufficiently small. Therefore, smaller concentration differences could be obtained by reducing further the size of the kernel support and increasing the number of neighbors. Hence as $n \to \infty$, the second-order error is governed by the kernel approximation and the size of h.

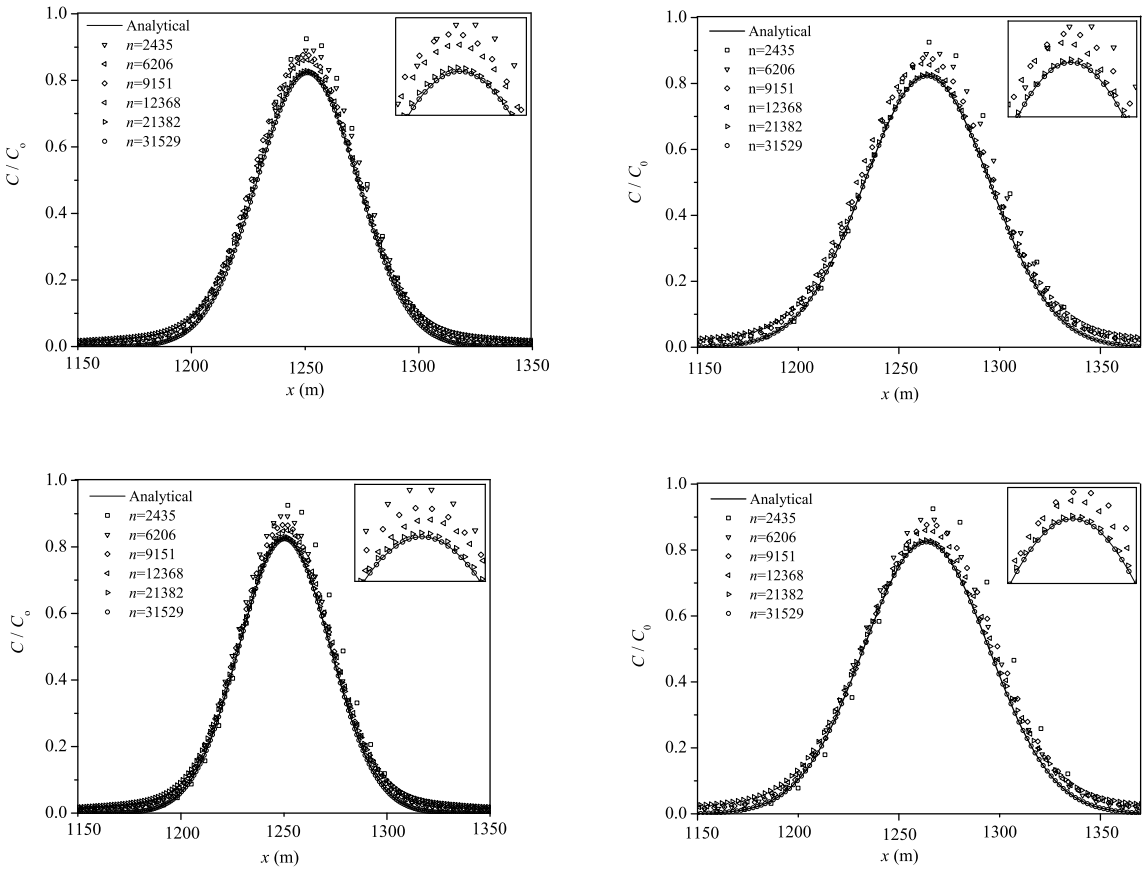

Figure 7: Concentration profiles at different spatial resolutions compared to the analytical solution (solid line) at $t = 300$ days for anisotropic dispersion with $\alpha_T/\alpha_L = 0.01$ and flow orientation $\theta = 0°$ (top left) and $\theta = 45°$ (top right), and with $\alpha_T/\alpha_L = 0.001$ and flow orientation $\theta = 0°$ (bottom left) and $\theta = 45°$ (bottom right).

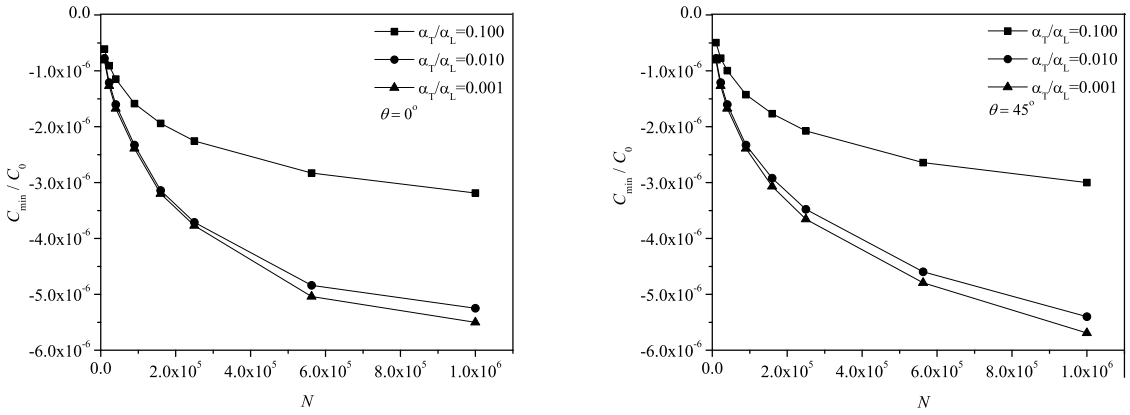

Figure 8: Maximum negative values of the concentration as a function of the total number of particles N for $\theta = 0°$ (left) and $\theta = 45°$ (right). The concentration is normalized with respect to the initial concentration C_0 and the results for all three dispersivity ratios are displayed.

Figure 7 compares the concentration profiles at different spatial resolutions with the analytical solution (solid line) at $t = 300$ days for anisotropic dispersion with $\alpha_{\mathrm{T}}/\alpha_{\mathrm{L}} = 0.01$ and flow orientation $\theta = 0°$ (top left) and $\theta = 45°$ (top right), and with $\alpha_{\mathrm{T}}/\alpha_{\mathrm{L}} = 0.001$ for $\theta = 0°$ (bottom left) and $\theta = 45°$ (bottom right). As in Fig. 3, all profiles are shown along a section inclined of 0° with respect to the x-axis. For both flow orientations and dispersion ratios, the numerical solution is seen to match the analytical profile for $N = 1000000$ and $n = 31529$. As the resolution is lowered, the numerical profiles become broader and their separation from the analytical solution increases around the peak of the distribution. As shown in Section 5.3, the worst RMSE between the numerical and analytical distributions at the highest resolution is $6.5 \times 10^{-4}\%$ and occurs for $\alpha_{\mathrm{T}}/\alpha_{\mathrm{L}} = 0.001$ and $\theta = 45°$. For comparison, when $\theta = 0°$ the deviation from the analytical profile is slightly smaller ($5.0 \times 10^{-4}\%$).

Negative concentrations are recurrently found in anisotropic transport models, not only in SPH simulations, but also with other particle methods and traditional mesh-based techniques [15]. When the off-diagonal components of the dispersion tensor are nonzero, the numerical solutions exhibit artificial oscillations, which amplify nonlinearly. Such oscillations induce negative values of the concentration, which represent serious limitations for

the correct prediction of anisotropic solute dispersion. According to previous SPH simulations, the situation worsens when the particles are distributed quasi-randomly. For example, for moderately large dispersivities ($\alpha_{\mathrm{T}}/\alpha_{\mathrm{L}} = 0.01$), Herrera and Beckie [15] reported maximum negative values of the concentration of $\approx -1.7 \times 10^{-2}$ kg m^{-3} ($\approx 5.3 \times 10^{-2} C_0$) for a quasi-random distribution. Although our simulations always predict positive concentrations for the isotropic scenario independently on the flow orientation, the same is not true for the anisotropic case. Figure 8 shows the magnitude of the maximum negative values as a function of the total number of particles for all three dispersion ratios when the particles are irregularly arranged (see Fig. 1). The results exhibit a negligible dependence on the flow direction as we may see by comparing the left ($\theta = 0°$) and right ($\theta = 45°$) plots. As expected, the smallest magnitudes at all resolutions occur for $\alpha_{\mathrm{T}}/\alpha_{\mathrm{L}} = 0.1$. In this case, the magnitude of the negative concentrations range from $\approx -4.9 \times 10^{-7} C_0$ for $N = 10000$ to $\approx -3.0 \times 10^{-6} C_0$ for $N = 1000000$. When the dispersivity is increased to $\alpha_{\mathrm{T}}/\alpha_{\mathrm{L}} = 0.01$ and 0.001, the magnitude of the maximum negative concentrations increases by a factor of 2, ranging from $\approx -8.1 \times 10^{-7} C_0$ for $N = 10000$ to $\approx -5.7 \times 10^{-6} C_0$ for $N = 1000000$ when $\alpha_{\mathrm{T}}/\alpha_{\mathrm{L}} = 0.001$. However, there is no much difference in the negative concentration values when increasing the dispersivity from 0.01 to 0.001. In all cases, the magnitude of the negative concentrations increases with increasing resolution, which is not surprising because at coarser resolution more numerical diffusion is added which causes more damping of the unphysical oscillations. However, at the highest resolutions the rate of increase of the magnitude of the negative concentrations slows down and so it appears that at even higher resolutions these magnitudes will stabilize toward a constant value. Compared to Herrera and Beckie [15], the present SPH scheme produces fewer negative concentrations than standard SPH, with maximum negative concentrations that are from 3 to 4 orders of magnitudes lower. However, Avesani *et al.* [16] reported a limit to the absolute value of negative concentrations less than about $10^{-7} C_0$ with their MWSPH scheme. In their case, concentrations and concentration gradients are computed at the midpoint of the segment connecting particle pairs, using local high-order reconstruction at the particle positions given the concentrations of the surrounding particles. Such non-oscillatory (WENO) reconstruction technique on moving points has proved to be efficient in drastically reducing the amplitude of the unphysical oscillations.

The top panels of Fig. 9 display the concentration fields at $t = 300$ days

for the anisotropic dispersion runs with $\alpha_T/\alpha_L = 0.1$ and 0.01 when $\theta = 45°$ using $N = 1000000$ and $n = 31529$ as compared to the analytical solution. The bottom panels show the case when $\alpha_T/\alpha_L = 0.001$ for $\theta = 0°$ (left) and 45° (right). At this resolution, all solutions exhibit negative concentrations represented by the white bands along the transversal direction on both sides of the plume elongation. We may see that the white bands are oriented parallel to the flow direction and always appear in the tail of the distributions where the concentration decays asymptotically to zero. The elliptic deformation and structure of the contaminant plume due to the anisotropic dispersion is remarkably similar to the analytical solution in all cases. Compared to standard SPH [15], the region occupied by the negative concentrations are now distributed over smaller portions of the computational domain and their widths are comparable to those from the accurate MWSPH results reported by Avesani *et al.* [16].

The gain in terms of accuracy of the MWSPH method is associated to an increase of the computational cost. In their Table 2, Avesani *et al.* [16] give the CPU time of their serial code for particles distributed uniformly within the domain on an Intel(R) Core(TM) i7-2640M CPU 2.80 GHz single processor. The CPU times in seconds for all resolutions with the present parallelized SPH code are given in the last column of Table 1. However, a comparison of the computational cost between the MWSPH code and the present scheme can only be done in an approximate sense. For instance, our parallelized code on an Intel(R) Xeon E5-2690 v3 CPU, with clockspeed 2.6 GHz and 12 cores will run about 100 times faster than a serial version on a single Intel(R) Core(TM) i7-2640M processor. Therefore, an inspection of Table 1 and their Table 2 shows that for similar resolutions the computational demand of both schemes is comparable. However, one advantage of the present SPH scheme is that it gives comparable accuracy to the MWSPH method with a much simpler approach.

For the isotropic case, Herrera and Beckie [15] found that the use of higher-order kernels does not provide a significant improvement of the numerical solution when the particles are regularly distributed. In contrast, the use of higher-order cutoff functions in the PSE method results in smaller errors with maximum magnitudes of the negative concentration values that range from less than 1% for second-order cutoff functions to less than 0.0003% of the maximum concentration for a fourth-order cutoff function [12]. However, for the anisotropic case, it was found that the use of higher-order SPH kernels has only a limited impact on removing the unphysical oscillations in

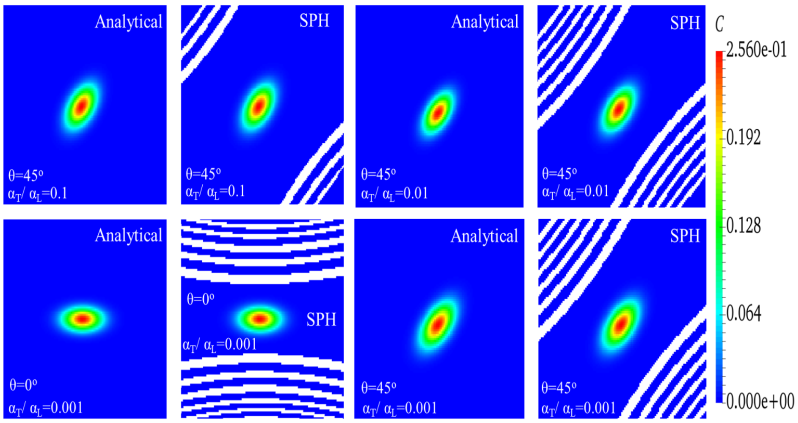

Figure 9: Concentration field resulting from the highest resolutions runs with $N = 1000000$ particles and $n = 31529$ neighbors as compared to the analytical solution at $t = 300$ days for $\alpha_{\mathrm{T}}/\alpha_{\mathrm{L}} = 0.1$ and 0.01 when $\theta = 45°$ (top panels) and $\alpha_{\mathrm{T}}/\alpha_{\mathrm{L}} = 0.001$ when $\theta = 0°$ and 45° (bottom panels). All anisotropic dispersion calculations exhibit negative concentrations in the transverse direction as shown by the white bands on each side of the solute plume. The color bar on the right indicates the magnitude of the concentration in kg m^{-3} for all frames.

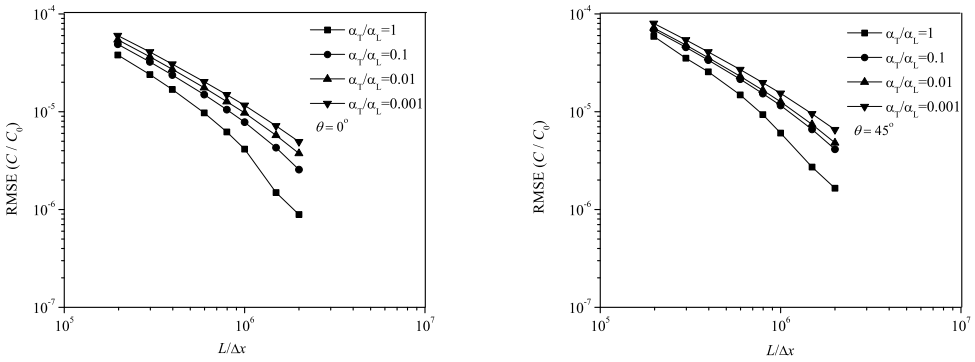

Figure 10: RMSE of the SPH numerical solutions as a function of $L/\Delta x$ for $\theta = 0°$ (left) and $\theta = 45°$ (right). The errors are shown for all dispersivity ratios.

the transverse direction [15].

5.3. SPH Errors and accuracy

We measure the accuracy of the numerical solutions by means of a root-mean-square error (RMSE)

$$\mathrm{RMSE}(C) = \sqrt{\frac{1}{N}\sum_{a=1}^{N}(C_a^{\mathrm{Anal}} - C_a^{\mathrm{SPH}})^2}, \tag{21}$$

which is closely related to the L_2-norm error. Since the SPH errors have a normal rather than a uniform distribution, the RMSE will provide a better representation of the error distribution than other statistical metrics [34]. In addition, the RMSE consists of squaring the magnitude of the errors before they are averaged, and so it gives a relatively higher weight to errors with large absolute values. Figure 10 shows the RMSE of the numerical concentrations normalized to the initial maximum concentration as a function of $L/\Delta x$ for $\theta = 0°$ (left) and $\theta = 45°$ (right), respectively. For the isotropic models ($\alpha_{\mathrm{T}}/\alpha_{\mathrm{L}} = 1.0$), the error declines as $\sim \Delta x^{2.02}$ for $\theta = 0°$ and as $\sim \Delta x^{1.94}$ for $\theta = 45°$. For anisotropic dispersion the convergence becomes slower than second-order with $\sim \Delta x^{1.76}$ for $\alpha_{\mathrm{T}}/\alpha_{\mathrm{L}} = 0.1$ to $\sim \Delta x^{1.30}$ for the more extreme case when $\alpha_{\mathrm{T}}/\alpha_{\mathrm{L}} = 0.001$ and $\theta = 0°$. Similar convergence rates are obtained for $\theta = 45°$, with the RMSEs varying from $\sim \Delta x^{1.71}$ for

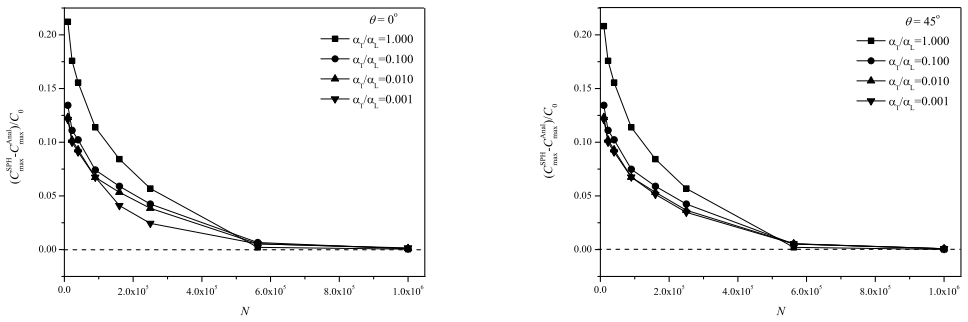

Figure 11: Difference of the maximum concentration values between the analytical and numerical solutions as a function of the total number of particles for $\theta = 0°$ (left) and $\theta = 45°$ (right). In both cases, the relative errors are shown for all spatial resolutions and dispersivity ratios.

$\alpha_T/\alpha_L = 0.1$ to $\sim \Delta x^{1.29}$ for $\alpha_T/\alpha_L = 0.001$. Thus, at relatively small particle spacing (i.e., large values of $L/\Delta x$), the rate of convergence is close to second-order for isotropic dispersion, meaning that C^1 particle consistency is achieved when $N \geq 562500$ and $n \geq 21382$. For moderately low dispersivities ($\alpha_T/\alpha_L = 0.1$), the convergence rate is also close to second-order, while for larger dispersivities ($\alpha_T/\alpha_L \leq 0.01$) the convergence rates slow down, though they are always better than first-order even in the most extreme case when $\alpha_T/\alpha_L = 0.001$. The approximate quadratic convergence for $\alpha_T/\alpha_L = 0.1$ is reassuring since this dispersion ratio is in line with what is indeed observed experimentally [3].

Figure 11 shows the dependence of the relative difference between the maximum numerical and analytical concentrations for $\theta = 0°$ (left) and $\theta = 45°$ (right). The results are shown for all resolutions and dispersion ratios. In all cases, the relative difference decreases as the resolution is increased. Good convergence to the analytical solution is always achieved for $N = 562500$ and $n = 21382$ independently of the flow orientation and dispersion ratio. As the resolution is further increased to $N = 1000000$ and $n = 31529$, the relative differences tend to zero with $C^{\mathrm{SPH}} - C^{\mathrm{Anal}} \approx 1.9 \times 10^{-4} C_0$ for $\alpha_T/\alpha_L = 1.0$, $\approx 7.2 \times 10^{-4} C_0$ for $\alpha_T/\alpha_L = 0.1$, $\approx 8.2 \times 10^{-4} C_0$ for $\alpha_T/\alpha_L = 0.01$, and $\approx 8.0 \times 10^{-4} C_0$ for $\alpha_T/\alpha_L = 0.001$.

For large anisotropic dispersion, the use of large numbers of neighbors results in lower errors and improved convergence rates as compared to stan-

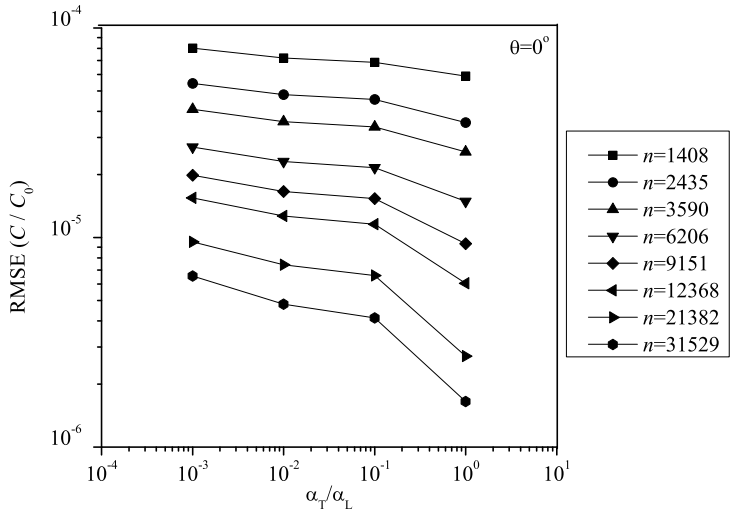

Figure 12: RMSE of the SPH numerical solutions as a function of the dispersivity ratio for $\theta = 0°$. A similar plot is obtained when $\theta = 45°$.

dard SPH. This can be better seen from Fig. 12, where the RMSEs are plotted versus the dispersion ratio $\alpha_{\mathrm{T}}/\alpha_{\mathrm{L}}$ for all models when $\theta = 0°$. An almost identical plot is obtained when the flow orientation is changed to $\theta = 45°$, a result which is consistent with the findings of previous dispersion simulations using equispaced particles. When passing from $N = 562500$ and $n = 21382$ to $N = 1000000$ and $n = 31529$, the RMSE is seen to decay more rapidly for isotropic than for anisotropic dispersion, while at low resolution the errors are almost constant for the range of dispersivity ratios considered. In the light of these results a reduction of the zeroth-order discretization errors that appear when passing from the continuous kernel to the particle approximation is enough to guarantee convergence for SPH simulations of anisotropic dispersion. Preliminary tests have shown that using smaller time steps and different scalings, leading to smaller values of h while maintaining large numbers of neighbors, have little effect on improving the convergence rate for large anisotropic dispersion. On the other hand, restoring consistency makes SPH to become insensitive to particle disorder [20]. This is true because for large numbers of neighbors within the kernel support, the SPH interpolation errors decrease independently of how the particles are dis-

tributed within the kernel support. Moreover, compared to more traditional kernels, the Wendland functions prevent the growth of particle disorder as they do not allow particle motion at sub-resolution scales, that is, at scales smaller than the smoothing length [31].

Equation (2) is the classical Fick's second law describing the diffusion and dispersion of a substance, and results from combining the continuity equation for the concentration and Fick's first law for the flux. It is well-known that due to its parabolic character, this equation issues an infinite velocity of propagation, which is clearly unphysical [35]. That is, according to its analytical solution (18), even for very small times there will always exist a finite amount of the diffusing and dispersing contaminant at large distances from the site where it was initially injected, implying an infinitely fast propagation. To overcome this difficulty, Cattaneo [36] proposed a modification by adding an *ad hoc* small term of the form $\tau d^2C/dt^2$ to the classical Fick's first law, which converts Eq. (2) into the more general form

$$\tau\frac{d^2C}{dt^2}+\frac{dC}{dt}=\nabla\cdot(\mathbb{D}\cdot\nabla C), \tag{22}$$

which is of a damped wave equation type, known as the telegrapher or Cattaneo's equation. While Fick's first law implies that the flux adjusts instantaneously to the gradient of the concentration, giving rise to an unrealistically infinitely fast spreading of local disturbances, the term $\tau d^2C/dt^2$ turns the ADE into a hyperbolic equation, where now the flux relaxes with some characteristic time constant τ. As a consequence, the propagation velocity along the longitudinal and transverse directions, namely $v_{\mathrm{p},i}=(D_{ii}/\tau)^{1/2}$, remains finite. This model has been successfully used to account for anomalous dispersion in amorphous materials [37], among many other applications that have been reported in the literature until recent years. In the singular limit $\tau\to 0$, $v_{\mathrm{p},i}\to\infty$ and so Eq. (22) reduces to Eq. (2). However, in passing we remind that hyperbolic equations may not preserve strict positivity. That is, even though $C(\mathbf{x},t)\geq 0$, the numerical solution of Eq. (22) may in general suffer from negative values [38]. In the framework of a consistent SPH scheme the problem then reduces to investigate under which conditions either Eq. (2) or Eq. (22) can be used to model anomalous transport for large anisotropy ratios while keeping the solution free from the numerical instabilities that lead to unphysical negative concentrations.

6. Conclusions

In this paper, we have proposed a consistent smoothed particle hydrodynamics (SPH) approach to simulate the anisotropic dispersion of a solute in porous media. Zeroth- and first-order consistency of the SPH scheme is achieved by setting the number of neighbors within the kernel support (n) and the size of the smoothing length (h) in terms of the total number of particles (N) by means of power-law relations of the form $n \propto N^{1-3/\beta}$ and $h \propto N^{-1/\beta}$ for $\beta \in [5, 7]$ [22], which satisfy the asymptotic limits $N \to \infty$, $h \to 0$ and $n \to \infty$, with $n/N \to 0$, for full particle consistency as N is increased [21]. The consistency and accuracy of SPH improves as the number of neighbors is increased and the size of the smoothing length is decreased with resolution, which is consistent with the expected dependence of the SPH discretization errors on $1/n$ [23, 24]. These errors contribute with zeroth-order terms that would persist when working with small numbers of neighbors even though $N \to \infty$ and $h \to 0$, leading to complete loss of consistency [24]. A Wendland C^4 function is employed for the kernel interpolation, which can support large numbers of particles without a pairing instability [30].

We test the performance of the consistent SPH scheme against the analytical solution of a two-dimensional benchmark test for the isotropic and anisotropic dispersion of a Gaussian plume in an external uniform flow using an irregular distribution of particles and compare with previous SPH simulations for the same test problem [15, 16]. As the number of particles and neighbors within the kernel support are increased, the distance between the numerical and analytical concentration solutions is reduced. Both solutions are seen to match independently of the flow orientation and dispersivity ratio when $N = 1000000$ and $n = 31590$, suggesting that these values may represent a lower limit for convergence of SPH for anisotropic transport. The numerical solutions exhibit convergence rates and magnitudes of the negative concentrations comparable to those reported by Avesani *et al.* [16] with their MWSPH method based on a Moving-Least-Squares-Weighted-Essentially-Non-Oscillatory (MLS-WENO) reconstruction of concentrations, which is at best one of the most accurate particle methods for approximating anisotropic dispersion. However, an advantage of the present method compared to MWSPH is its simplicity. Any user working with standard SPH can easily modify his/her code to improve convergence and accuracy on dispersion problems. This aspect is of significance for most practical applications where prediction of local-scale dispersion on plume movement, mixing and

dilution are important. The same is true for applications of solute dispersion in multiphase flows and reactive transport.

Up to the level of resolution tried here, the solutions are not free from unphysical oscillations that induce negative values of the concentrations. However, the use of large numbers of neighbors coupled to small kernel supports results in negative concentration values that are several orders of magnitude lower than predicted by standard SPH simulations [15] and comparable to those from accurate MWSPH simulations [16]. Evidently, restoring approximate first-order consistency for the particle approximation is not enough to ensure a full positive solution for anisotropic dispersion. The apparently irreducible problem associated with the unphysical oscillations for highly anisotropic dispersion must not be necessarily attributed to intrinsic deficiencies of the numerical method but rather to the parabolic character of the classical Fick's second law, which issues an infinite velocity of propagation, giving rise to an unrealistically infinitely fast spreading of local disturbances at large distances from the site where they were initially injected.

acknowledgements

The calculations of this paper were performed using the computational facilities of the ABACUS-Centro de Matemática Aplicada y Cómputo de Alto Rendimiento of Cinvestav. We acknowledge finantial support from the Conacyt-Sener Energy Sustainability Strategic Project No. 212602 (AZTLAN Platform). One of us (L. Di G. S.) acknowledges support from the Universidad Autónoma Metropolitana - Azcapotzalco (UAM-A) through internal funds.

7. Bibliography

[1] J. Lewis, J. Sjostrom, Optimizing the experimental design of soil columns in saturated and unsaturated transport experiments, J. Contam. Hydrol. (2010), 115: 1–4 https://doi.org/10.1016/j.jconhyd.2010.04.001.

[2] R.J. Parkinson, P. Griffiths, A.L. Heathwaite, Transport of nitrogen in soil water following the application of animal manures to sloping grassland, Hydrol. Sci. J. (2000), 45(1): 61–73 https://doi.org/10.1080/02626660009492306.

[3] J. Bear, Dynamics of Fluids in Porous Media, Dover, New York, 1988.

[4] T.G. Poulsen, W. Suwarnarat, M.K. Hostrup, P.N.V. Kalluri, Simple and rapid method for measuring gas dispersion in porous media: methodology and applications, Soil Sci. 173(3): 169–174 https://doi.org/10.1097/SS.0b013e31816408c9.

[5] A.G. Hunt, T.E. Skinner, Predicting dispersion in porous media, Complexity (2010), 16(1): 43–55 https://doi.org/10.1002/cplx.20322.

[6] P. Sharma, T.G. Poulsen, Gas dispersion and immobile gas content in granular porous media: effect of particle size nonuniformity, Soil Sci. (2010), 175(9): 426–431 https://doi.org/10.1097/SS.0b013e3181f0edaf.

[7] C. Le Potier, Finite volume monotone scheme for highly anisotropic diffusion operators on unstructured triangular meshes, Comptes Rendus Math. (2005), 341(12): 787-792 https://doi.org/10.1016/j.crma.2005.10.010.

[8] J.M. Nordbotten, I. Aavatsmark, Monotonicity conditions for control volume methods on uniform parallelogram grids in homogeneous media, Comput. Geosci. (2005), 9(1): 61–72 https://doi.org/10.1007/s10596-005-5665-2.

[9] M.J. Mlacnik, L.J. Durlofsky, Unstructured grid optimization for improved monotonicity of elliptic equations with highly anisotropic coefficients, J. Comput. Phys. (2006), 216(1): 337–361 https://doi.org/10.1016/j.jcp.2005.12.007.

[10] G. Yuan, Z. Sheng, Monotone finite volume schemes for diffusion equations on polygonal meshes, J. Comput. Phys. (2008), 227(12): 6288–6312 https://doi.org/10.1016/j.jcp.2008.03.007.

[11] K. Lipnikov, D. Svyatskiy, Y. Vassilevski, Interpolation-free monotone finite volume method for diffusion equations on polygonal meshes, J. Comput. Phys. (2009), 228(3): 703–716 https://doi.org/10.1016/j.jcp.2009.09.031.

[12] S. Zimmermann, P. Koumoutsakos, W. Kinzelbach, Simulation of pollutant transport using a particle method, J. Comput. Phys. (2001), 173(1): 322–347 https://doi.org/10.1006/jcph.2001.6879.

[13] A. Beaudoin, S. Huberson, E. Rivoalen, Simulation of anisotropic diffusion by means of a diffusion velocity method, J. Comput. Phys. (2003), 186(1): 122–135 https://doi.org/10.1016/S0021-9991(03)00024-X.

[14] P. A. Herrera, M. Massabó, R.D. Beckie, A meshless method to simulate solute transport in heterogeneous porous media, Adv. Water Resour. (2009), 32: 413–429 https://doi.org/10.1016/j.advwatres.2008.12.005.

[15] P.A. Herrera, R.D. Beckie, An assessment of particle methods for approximating anisotropic dispersion, Int. J. Numer. Meth. Fluids (2013), 71: 634–651 https://doi.org/10.1002/fld.3676.

[16] D. Avesani, P. Herrera, G. Chiogna, A. Bellin, M. Dumbser, Smooth particle hydrodynamics with nonlinear moving-least-squares WENO reconstruction to model anisotropic dispersion in porous media, Adv. Water Resour. (2015), 80: 43–59 http://dx.doi.org/10.1016/j.advwatres.2015.03.007.

[17] P. Degond, S. Mas-Gallic, The weighted particle method for convection-diffusion equations. Part 2: The anisotropic case, Math. Comput. (1989), 53(188): 509–525 https://doi.org/10.2307/2008717.

[18] P. Degond, F.-J. Mustieles, A deterministic approximation of diffusion equations using particles, SIAM J. Sci. Stat. Comput. (1990), 11(2): 293–310 https://doi.org/10.1137/0911018.

[19] P.W. Cleary, J.J. Monaghan, Conduction modelling using smoothed particle hydrodynamics, J. Comput. Phys. (1999), 148(1): 227–264 https://doi.org/10.1006/jcph.1998.6118.

[20] L. Di G. Sigalotti, J. Klapp, O. Rendón, C.A. Vargas, F. Peña-Polo, On the kernel and particle consistency in smoothed particle hydrodynamics, Appl. Numer. Math. (2016), 108: 242–255 http://dx.doi.org/10.1016/j.apnum.2016.05.007.

[21] F.A. Rasio, Particle methods in astrophysical fluid dynamics, Prog. Theoret. Phys. Suppl. (2000), 138: 609–621 https://doi.org/10.1143/PTPS.138.609.

[22] Q. Zhu, L. Hernquist, Y. Li, Numerical convergence in smoothed particle hydrodynamics, Astrophys. J. (2015), 800:6 (13pp) https://doi.org/10.1088/0004-637X/800/1/6.

[23] J.J. Monaghan, Smoothed particle hydrodynamics, Annu. Rev. Astron. Astrophys. (1992), 30: 543–574 https://doi.org/10.1146/annurev.aa.30.090192.002551.

[24] J.I. Read, T. Hayfield, O. Agertz, Resolving mixing in smoothed particle hydrodynamics, Mon. Not. R. Astron. Soc. (2010), 405(3): 1513–1530 https://doi.org/10.1111/j.1365-2966.2010.16577.x.

[25] A.E. Scheidegger, General theory of dispersion in porous media, J. Geophys. Res. (1961), 66(10): 3273–3278 https://doi.org/10.1029/JZ066i010p03273.

[26] M. Yildiz, R.A. Rook, A. Suleman, SPH with multiple boundary tangent method, Int. J. Numer. Meth. Eng. (2009), 77(10): 1416–1438 https://doi.org/10.1002/nme.2458.

[27] J.P. Morris, P.J. Fox, Y. Zhu, Modeling low Reynolds number incompressible flows using SPH, J. Comput. Phys. (1997), 136(1): 214–226 https://doi.org/10.1006/jcph.1997.5776.

[28] M.B. Liu, G.R. Liu, Restoring particle consistency in smoothed particle hydrodynamics, Appl. Numer. Math. (2006), 56(1): 19–36 https://doi.org/10.1016/j.apnum.2005.02.012.

[29] H. Wendland, Piecewise polynomial, positive definite and compactly supported radial functions of minimal degree, Adv. Comput. Math. (1995), 4(1): 389–396 https://doi.org/10.1007/BF02123482.

[30] W. Dehnen, H. Aly, Improving convergence in smoothed particle hydrodynamics without pairing instability, Mon. Not. R. Astron. Soc. (2012), 425(2): 1068–1082 https://doi.org/10.1111/j.1365-2966.2012.21439.x.

[31] S. Rosswog, SPH methods in the modelling of compact objects, Living Rev. Comput. Astrophys. (2015), 1:1 https://doi.org/10.1007/lrca-2015-1.

[32] M. Gómez-Gesteira, B.D. Rogers, A.J.C. Crespo, R.A. Dalrymple, M. Narayanaswamy, J.M. Domínguez, Sphysics-development of a free-surface fluid solver – Part 1: Theory and formulations, Comput. Geosci. (2012), 48: 289–299.

[33] A.J.C. Crespo, J.M. Domínguez, B.D. Rogers, M. Gómez-Gesteira, S. Longshaw, R. Canelas, R. Vacondio, A. Barreiro, O. García-Feal, Dualsphysics: Open-source parallel cfd solver based on smoothed particle hydrodynamics (sph), Comput. Phys. Commun. (2015), 187: 204–216.

[34] T. Chai, R.R. Draxler, Root mean square error (RMSE) or mean absolute error (MAE)? – Arguments against avoiding RMSE in the literature, Geosci. Model Dev. (2014), 7(3): 1247–1250 https://doi.org/10.5194/gmd-7-1247-2014.

[35] A. Compte, R. Metzler, The generalized Cattaneo equation for the description of anomalous transport processes, J. Phys. A: Math. Gen. (1997), 30(21): 7277–7289 https://doi.org/10.1088/0305-4470/30/21/006.

[36] C. Cattaneo, Sulla conduzione del calore, Atti Semin. Mat. Fis. Univ. Modena e Reggio Emilia (1948), 3: 83–101.

[37] H. Scher, E.W. Montroll, Anomalous transit-time dispersion in amorphous solids, Phys. Rev. B (1975), 12: 2455–2477 https://doi.org/10.1103/PhysRevB.12.2455.

[38] V. Mendez, S. Fodotov, W. Horsthemke, Reaction-Transport Systems: Mesoscopic Foundations, Fronts, and Spatial Instabilities, Springer, Berlin, 2010.